Editors' Suggestion

High-Stability Single-Ion Clock with 5.5×10^{-19} Systematic Uncertainty

Mason C. Marshall,[1,*] Daniel A. Rodriguez Castillo,[1,2] Willa J. Arthur-Dworschack,[1,2] Alexander Aeppli,[2,3] Kyungtae Kim,[2,3] Dahyeon Lee,[2,3] William Warfield,[2,3] Joost Hinrichs,[1,4] Nicholas V. Nardelli,[1] Tara M. Fortier,[1] Jun Ye,[2,3] David R. Leibrandt,[1,2,5] and David B. Hume[1,2,†]

[1]*Time and Frequency Division, National Institute of Standards and Technology, Boulder, Colorado, USA*
[2]*Department of Physics, University of Colorado, Boulder, Colorado, USA*
[3]*JILA, National Institute of Standards and Technology and the University of Colorado, Boulder, Colorado, USA*
[4]*Institute of Quantum Optics, Leibniz University Hannover, Hannover, Germany*
[5]*Department of Physics and Astronomy, University of California, Los Angeles, California, USA*

(Received 25 April 2025; accepted 17 June 2025; published 14 July 2025)

We report a single-ion optical atomic clock with a fractional frequency uncertainty of 5.5×10^{-19} and fractional frequency stability of $3.5 \times 10^{-16}/\sqrt{\tau/\mathrm{s}}$, based on quantum logic spectroscopy of a single $^{27}Al^+$ ion. A cotrapped $^{25}Mg^+$ ion provides sympathetic cooling and quantum logic readout of the $^{27}Al^+$ $^1S_0 \leftrightarrow {}^3P_0$ clock transition. A Rabi probe duration of 1 s, enabled by laser stability transfer from a remote cryogenic silicon cavity across a 3.6 km fiber link, results in a threefold reduction in instability compared to previous $^{27}Al^+$ clocks. Systematic uncertainties are lower due to an improved ion trap electrical design, which reduces excess micromotion, and a new vacuum system, which reduces collisional shifts. We also perform a direction-sensitive measurement of the ac magnetic field due to the rf ion trap, eliminating systematic uncertainty due to field orientation.

DOI: 10.1103/hb3c-dk28

Introduction—Optical atomic clocks based on spectroscopy of dipole-forbidden electronic transitions in isolated, trapped atoms are among the most precise instruments developed, capable of measuring time more precisely than the cesium clocks that currently define the second [1]. Accordingly, optical clock frequency ratios are some of the most accurate measurements [2,3] and are used as probes for new physics [4], including time variation of fundamental constants [5,6]; violations of local position invariance [7]; constraints on dark matter [2,8,9]; and general relativity at small scales [10,11]. Optical clocks based on single trapped ions [12,13] and neutral atoms in optical lattices [14] have reached fractional frequency uncertainties below 10^{-18}; further advances open new possibilities for these investigations. Additionally, as the scientific community moves toward the redefinition of the second, advances in the state of the art for clock accuracy and stability are critical [15].

The exquisite degree of control and access to environmentally insensitive transitions offered by trapped atomic ions have made them a leading technology for measurement accuracy. In particular, the $^1S_0 \leftrightarrow {}^3P_0$ transition in singly ionized aluminum offers a high transition frequency, long excited-state lifetime, and one of the lowest known sensitivities to blackbody radiation [16–19]. In this Letter, we report the accuracy and stability evaluation of the current-generation $^{27}Al^+$ quantum logic clock at the National Institute of Standards and Technology (NIST). This clock realizes the lowest fractional frequency uncertainty of any clock to date, at $\Delta\nu/\nu = 5.5 \times 10^{-19}$. Its fractional instability of $3.5 \times 10^{-16}/\sqrt{\tau/\mathrm{s}}$ represents a threefold reduction in instability compared to the previous NIST quantum logic clock [12]. Critical to these achievements are a more stable clock laser, an improved Paul trap electrical design with reduced excess micromotion, and a 150× improvement in background gas pressure from a new ultrahigh vacuum system.

Clock operation and stability—The operation of the clock is similar to that described in [12,20]. The clock cycle begins with preparation of the $^{27}Al^+$ clock ion into one of the $|{}^1S_0, m_F = \pm 5/2\rangle$ states via optical pumping on the $^1S_0 \leftrightarrow {}^3P_1$ transition. Sympathetic cooling on the $^{25}Mg^+$ logic ion then brings the ion pair to the Doppler temperature limit. Finally, we probe the $^{27}Al^+$ clock transition using Rabi spectroscopy followed by quantum logic readout [21,22].

We probe both the $m_F = +5/2$ and $m_F = -5/2$ $^1S_0 \leftrightarrow {}^3P_0$ transitions and generate a "virtual" first-order magnetic-field-insensitive transition from their mean frequency [23]. Additionally, we alternate probing from opposite directions, with the two probe beams counterpropagating through the same single-mode optical fibers; the average of opposite directions is insensitive to possible first-order

*Contact author: mason.marshall@nist.gov
†Contact author: david.hume@nist.gov

Doppler shifts due to ion motion. Both probe laser acousto-optic modulators (AOMs) are switched on during each cycle, with the inactive direction detuned by 100 kHz. This maintains a nearly identical electric- and magnetic-field environment for probes in either direction and either side of the $^{27}Al^+$ Zeeman structure.

Decoherence of the $^{27}Al^+$ clock laser ($\lambda_L \simeq 267$ nm) limited previous generations to a 150 ms probe time. We extend the laser coherence by transferring the stability of the JILA cryogenic silicon cavity [24] to the clock laser. An ultrastable laser locked to this cavity travels over a 3.6 km path-length-stabilized fiber link to NIST. This fiber link via the Boulder Research and Administrative Network has been described previously [2]; for this work, it has been modified as shown in Fig. 1(a), such that the cavity-stabilized light serves as reference for an Er:Yb frequency comb [25,26]. We first prestabilize the $^{27}Al^+$ clock laser with a Pound-Drever-Hall lock to a room-temperature ultralow-expansion glass cavity. With a lower bandwidth of ~10 kHz, we then modulate the drive frequency of an AOM to stabilize the beat note between clock laser and frequency comb. With this improved clock-laser stabilization, we can operate the clock using a 1 s probe duration without substantial loss of atom-laser coherence.

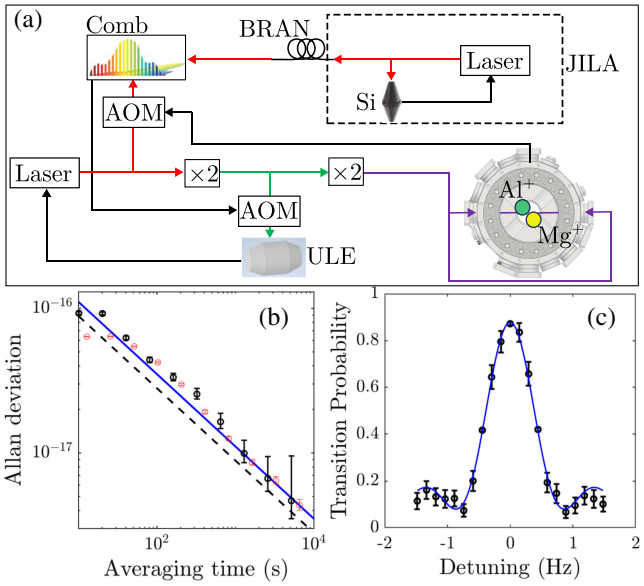

FIG. 1. (a) Schematic of the optical network for laser stability transfer between the JILA silicon cavity and the Al^+ clock laser. See the text for details. Black lines represent electronic feedback; all others represent path-length-stabilized laser beam paths. BRAN: Boulder Research and Administrative Network (3.6 km fiber link); AOM: acousto-optic modulator used for frequency stabilization; Si: cryogenic silicon cavity; ×2: frequency doubling stage; ULE: room-temperature ultralow-expansion glass cavity. (b) Overlapping Allan deviation of the frequency ratio ν_{Al^+}/ν_{Sr} (black points). Asymptotic fit (blue line) gives a fractional frequency stability of $3.5 \times 10^{-16}/\sqrt{\tau/s}$ beyond the servo time of ~80 s (where τ is the averaging time). The dashed line represents the projection noise limit. Red points are overlapping Allan deviation of a simulation incorporating experimental noise and duty cycle. Error bars are 68% confidence interval of Allan deviation. (c) $^{27}Al^+$ clock transition line shape with a 1 s probe. Error bars are 68% binomial confidence interval of transition probability.

To operate with a 1 s probe, we control effects which scale with the probe time. Previous $^{27}Al^+$ clocks have been operated by ground-state cooling before the clock probe [27]; however, with a 1 s probe time, the heating rate in our system would yield average motional phonon occupation numbers above the Doppler limit. We therefore Doppler cool the logic ion during the clock probe and carefully characterize the temperature at the Doppler limit.

Since Doppler cooling produces a thermal distribution [28,29], we expect the main nonthermal component to arise from collisions with background gas, which are accounted for in the collision shift [30]. The probability of a collision between the trapped ions and background gas scales linearly with the probe time. To reduce the collision rate, we developed an all-titanium vacuum system to minimize hydrogen outgassing, as well as designing for improved conductance and hydrogen pumping speed. These improvements yielded a base pressure of $(2.5 \pm 1.3) \times 10^{-10}$ Pa $[(1.8 \pm 0.9) \times 10^{-12}$ Torr] as measured by the reorder rate of a two-ion crystal [31], sufficient to suppress the collision effect for long probe times. This also reduces the rate of aluminum hydride formation, decreasing the need to stop the clock and reload ions during a measurement run.

In addition to readout and state preparation, auxiliary operations are interleaved with clock interrogation to stabilize the ion order and measure the intensity of the cooling light. The clock interrogation has a duty cycle of ~80%. The clock-laser path length is stabilized through all optical fibers from the frequency comb to the trap vacuum chamber. An active magnetic field servo with ~1 kHz bandwidth adjusts shim coils surrounding the optical table based on flux gate sensors located on opposite sides of the vacuum chamber; this stabilizes the quantization field and minimizes noise at 60 Hz and harmonics.

We measure the $^{27}Al^+$ clock stability by comparison to the JILA Sr optical lattice clock [14], with results shown in Fig. 1(b). The optical lattice clock fractional stability is $< 1 \times 10^{-16}/\sqrt{\tau/s}$, meaning the comparison stability of $3.5 \times 10^{-16}/\sqrt{\tau/s}$ is dominated by the $^{27}Al^+$ clock. To our knowledge, this represents the lowest instability of any ion clock reported to date [3]. In the future, this stability could be improved by further extending the probe time using differential spectroscopy [36] or by extending the quantum logic clock to multiple spectroscopy ions [37–39].

In the following paragraphs, we describe the evaluation of systematic shifts to the $^{27}Al^+$ clock transition, as reported in Table I.

Secular motion—The relativistic time-dilation shift, or second-order Doppler shift, due to secular motion in the ion

TABLE I. Fractional frequency shifts and uncertainties for the NIST $^{27}Al^+$ quantum logic clock.

Effect	Shift (10^{-19})	Uncertainty (10^{-19})
Secular motion	−114.6	3.8
dc quad. Zeeman	−6317.9	2.5
Cooling laser Stark	−37.2	2.0
Blackbody radiation	−30.7	1.7
Excess micromotion	−1.6	1.6
Clock laser Stark	0	0.8
Background gas collisions	−0.3	0.4
ac quad. Zeeman	−0.54	0.06
First-order Doppler	0	< 1
AOM phase chirp	0	< 1
Electric quadrupole	0	< 1
Total	−6502.8	5.5

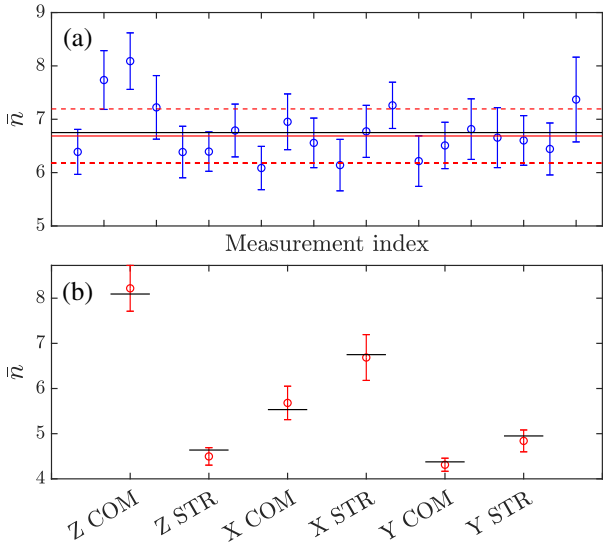

FIG. 2. (a) Repeated measurements of the motional quantum number for one of the radial stretch modes, performed over several months. Error bars are 1σ uncertainty. Red solid and dashed lines are the weighted mean and standard deviation of the measurements, respectively. The black line is the calculated Doppler limit for our nominal trap and laser parameters. (b) Weighted means and standard deviations for all six modes. Z modes are along the trap axis; X and Y modes are radial. STR: stretch; COM: center of mass. Black lines are the calculated Doppler limit for each mode.

trap [29] is the largest source of systematic uncertainty in this clock. We evaluate the energy in the secular modes of the two-ion crystal using sideband thermometry [40,41]. To quantify the statistical uncertainty and test the repeatability of sideband thermometry at the Doppler limit, we repeat the measurements many times over the course of several months. The results are consistent within the measurement uncertainty with the calculated Doppler limit for our nominal laser geometry and secular mode frequencies. Figure 2 shows the record of measurements for one of the radial "stretch" modes, with the others shown in Supplemental Material [31].

We controlled for potential systematic shifts in this temperature measurement by varying sideband pulse duration, altering the motional frequency spectrum and using higher-order sidebands for the analysis. We found no significant dependence of the results on any of these changes. We take the weighted standard deviation of all measurements for each secular mode to be the uncertainty on that mode's temperature. This accounts for possible instability in the underlying value as well as statistical uncertainty in the individual measurements. Since the uncertainties for each mode are statistical, we add them in quadrature to get a total secular motion shift of $\Delta\nu/\nu = -(114.6 \pm 3.8) \times 10^{-19}$.

Quadratic Zeeman shift—While the first-order Zeeman shift is eliminated by averaging transitions with opposite magnetic-field dependence, there remains a quadratic Zeeman shift. We write this as $\Delta\nu/\nu = C_2\langle B^2\rangle$, where C_2 is the quadratic Zeeman coefficient [42] and $\langle B^2\rangle = \langle B_{DC}\rangle^2 + \langle B_{AC}^2\rangle$. The frequency difference between Zeeman levels gives a real-time measure of the quantization field B_{DC}, while B_{AC} is measured via hyperfine spectroscopy on the $^{25}Mg^+$ ion [31]. The average dc quadratic Zeeman shift is $\Delta\nu/\nu = -(6317.9 \pm 2.5) \times 10^{-19}$, where the exact value for any given day of operation depends on the measured B_{DC}, but the uncertainty is not affected at the given level of precision. Compared to the previous-generation $^{27}Al^+$ clock, we operate at a lower magnetic field of 0.10 mT, which reduces the amplitude and uncertainty of the dc quadratic Zeeman shift.

$\langle B_{AC}^2\rangle$ is dominated by the magnetic field due to the trap rf drive at $\Omega/2\pi = 70.86$ MHz. We measure $\langle B_{AC}^2\rangle$ by observing a frequency shift on the first-order field-insensitive transition $|F = 3, m_F = 0\rangle \leftrightarrow |F = 2, m_F = 0\rangle$ in the $^{25}Mg^+$ ground state as a function of rf drive power, while using the first-order sensitive transition $|F = 3, m_F = -3\rangle \leftrightarrow |F = 2, m_F = -2\rangle$ to subtract $\langle B_{DC}\rangle^2$ [42]. This measurement is sensitive to the direction of the ac magnetic field relative to the quantization axis [43]. To remove this directional ambiguity, we repeat the measurement with the quantization axis oriented in three nearly orthogonal directions. We use three pairs of magnetic-field coils to change the magnetic-field direction and propagate the 280 nm laser beams used for $^{27}Mg^+$ state preparation and readout along each quantization axis. In each of these three conditions, we measure the hyperfine frequency shift at a range of different trap rf drive powers. Simultaneously fitting the results gives the ac quadratic Zeeman shift without directional ambiguity, where we quantify the uncertainty using a parametric bootstrapping method [44]. At our operating condition, this is $\langle B_{AC}^2\rangle = 0.85 \pm 0.09\ \mu\mathrm{T}^2$; this corresponds to a clock frequency shift of $\Delta\nu/\nu = -(0.54 \pm 0.06) \times 10^{-19}$. Figure 3 shows the

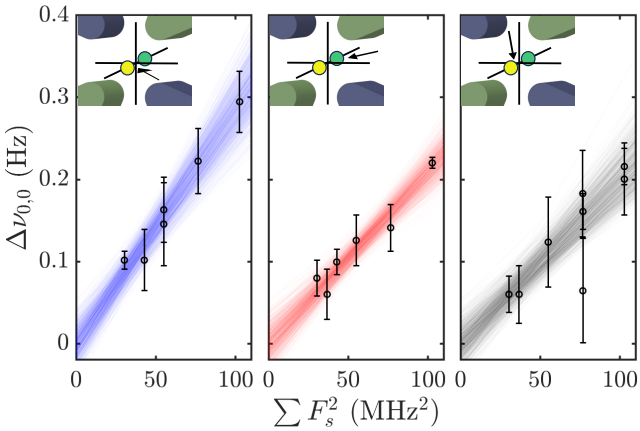

FIG. 3. Frequency shift on the $^{25}Mg^+|F=3,m_F=0\rangle \leftrightarrow |F=2,m_F=0\rangle$ ground-state hyperfine transition due to the trap-induced ac magnetic field. This shift is linear with $\langle B_{AC}^2\rangle$ and here plotted as a function of trap rf power, represented by the sum of squared trap secular frequencies ΣF_s^2. Error bars are 1σ uncertainty. The quantization field and detection laser are oriented along three nearly orthogonal axes; directions are nearly vertical or at 45° to the trap axis. These three axes are depicted as arrows in each inset, together with trap rf electrodes. Also shown are a subset of fit results from parametric bootstrapping of the measurement data and the angle of the near-orthogonal axes; see the text and [31].

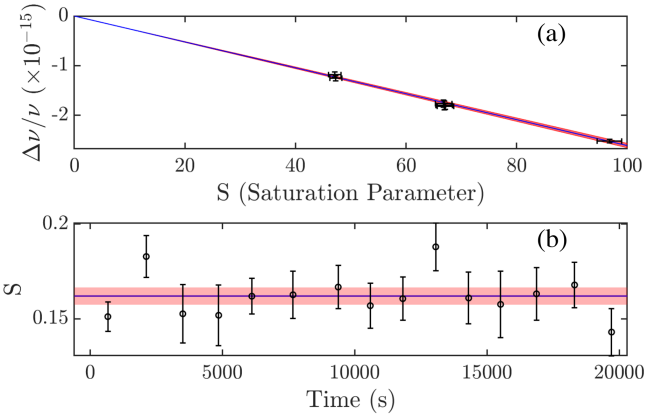

FIG. 4. Stark shift due to cooling light. (a) Six measurements of the frequency shift on the clock transition were performed at three different Stark shifting beam powers. Error bars are 1σ uncertainty. The blue line and red shaded region give the mean shift per saturation parameter and its weighted standard deviation, respectively. (b) Time series of saturation parameters measured during a day of clock operation, showing no evidence of long-term drift. Error bars are 1σ. The blue line and red shaded region are the saturation parameter and its 1σ uncertainty, $S = 0.1621 \pm 0.0046$, respectively, extracted from fitting the full day of data.

measured frequency shifts, as well as a subset of the simultaneous fit results projected back onto the three measurement axes. See Supplemental Material [31] for more details.

Cooling laser Stark shift—The 280 nm laser beam used for continuous Doppler cooling of the logic ion also illuminates the $^{27}Al^+$ spectroscopy ion, inducing an ac Stark shift. We evaluate this shift by directly measuring the Stark shift on the clock transition induced by a stronger 280 nm beam and then extrapolating to the lower power we use for Doppler cooling. Specifically, we measure the Stark shift on the clock transition from one of our 280 nm $^{25}Mg^+$ Raman beams, typically used for resolved-sideband cooling and quantum logic operations. While the Raman and Doppler beams are detuned from one another by ~50 GHz, this is small compared to the detuning from the deep UV transitions that dominate the clock transition differential polarizability [45]; the difference in Stark shift is, therefore, negligible.

The Rabi rates of Raman transitions, together with power ratios between beams in a Raman pair, give an absolute calibration of the saturation parameter S of the Stark shifting beam; see Supplemental Material [31] for more details. We measure at several different Stark-shifting beam powers, as shown in Fig. 4(a), obtaining a shift of $\Delta\nu/\nu = -(2.59 \pm 0.06) \times 10^{-17} \times S$.

During clock operation, we regularly measure the depumping rate of the $^{25}Mg^+$ qubit dark state to determine the saturation parameter. We apply a correction based on the average measurement across the day and the calibrated ratio of laser powers at the two ions' positions. Figure 4(b) shows measurements across a typical day of operation, binned into approximately 20-min intervals. In the absence of any long-term drift, we take the full day's worth of saturation parameter measurements and apply an average correction to the day's clock data. Repeating this procedure across many days of clock operation, we obtain an average shift and uncertainty of $\Delta\nu/\nu = -(37.2 \pm 2.0) \times 10^{-19}$, where the exact value for any given day of operation depends on the measured saturation parameter.

Blackbody radiation—The $^{27}Al^+$ clock transition has one of the lowest polarizabilities due to blackbody radiation of any existing atomic clock [16]. This was recently measured [46] with high precision in a $^{27}Al^+$-$^{40}Ca^+$ clock, using the Stark shift on the $^{40}Ca^+$ clock transition as a reference for the intensity of a Stark-shifting infrared laser and giving a polarizability of $(6.86 \pm 0.23) \times 10^{-42}$ Jm^2/V^2. We measure the temperature of our apparatus using a set of six thermocouples—three located on the trap and support structure and three on the surrounding vacuum chamber—constraining the ion's blackbody environment to be 24.0 ± 3.3°C, for a Stark shift due to blackbody radiation of $\Delta\nu/\nu = -(30.7 \pm 1.7) \times 10^{-19}$.

Excess micromotion—Excess micromotion (EMM) was the largest systematic uncertainty in the previous NIST $^{27}Al^+$ clock [12]. This is substantially reduced due to an improved Paul trap electrical design, featuring a thicker diamond wafer, thicker sputtered gold traces, and rerouting of the traces to balance capacitances on opposite rf

electrodes. We optimize micromotion compensation voltages at the start of each day of clock operation and measure again at the end of each day. These measurements constrain the EMM-induced second-order Doppler shift on the clock transition to $\Delta\nu/\nu = (-1.6 \pm 1.6) \times 10^{-19}$; see Supplemental Material [31] for more details on trap design and EMM constraints.

Background gas collisions—Frequency shifts due to background gas collisions in a $^{27}Al^{+}$ clock were evaluated in detail in [30], where a strong suppression of Doppler shifts due to collision-induced heating was identified, thanks to the Debye-Waller effect. The application of continuous Doppler cooling in this work weakens this suppression, as ions which would otherwise not interact with the clock laser are recooled during the probe time. However, the low pressure in our new vacuum system also strongly suppresses this shift. Accounting for the weaker Debye-Waller suppression, the measured collision rate, and the one-second probe time, we constrain this shift to be $\Delta\nu/\nu = -(0.25 \pm 0.36) \times 10^{-19}$. See [31] for additional details.

First-order Doppler shift—The previous-generation quantum logic clock observed a first-order Doppler shift on the order of 5×10^{-17}, which was strongly suppressed by averaging clock probes from opposite spatial directions. In this apparatus, we measure a first-order Doppler shift consistent with zero, at $\Delta\nu/\nu = (0.1 \pm 1.7) \times 10^{-18}$. Combined with the suppression from averaging opposite probe directions [12], the residual first-order Doppler shift is negligible.

Other shifts—A possible ac Stark shift due to the clock laser has been investigated, following [12,20]. Because of the lower laser intensity required for a one-second probe, the shift uncertainty is reduced to $\Delta\nu/\nu = \pm 0.8 \times 10^{-19}$. Possible AOM phase chirp effects and electric quadrupole shifts are also bounded below 10^{-19} [47].

Conclusion—We have developed a $^{27}Al^{+}$ clock with instability of $3.5 \times 10^{-16}/\sqrt{\tau/\mathrm{s}}$ and inaccuracy of 5.5×10^{-19}. This represents a threefold improvement in stability over previous aluminum ion clocks, while also advancing the state of the art in optical clock accuracy. The stability could be improved with an even more stable clock laser, enabling longer probe times, or by simultaneous interrogation of a Coulomb crystal including several aluminum ions. The accuracy is mainly limited by the measurement of the Doppler temperature. We note that a cryogenic system with low heating rates would allow ground-state operation with 1 s or longer probe times, while also reducing uncertainty due to background gas collisions and blackbody radiation. Combined with realistic improvements to the measurement of the quadratic Zeeman coefficient and micromotion amplitude, a clock with accuracy at the 1×10^{-19} level is feasible.

Acknowledgments—We thank S. M. Brewer for early design work on the trap and vacuum system; A. Contractor for contributions to the ion fluorescence imaging system; and C.-W. Chou for work on the saturation parameter measurement formalism and for useful discussions. We thank L. Sonderhouse and S. Scheidegger for careful reading of the manuscript. We acknowledge support from the Office of Naval Research; the National Institute of Standards and Technology; the National Science Foundation Q-SEnSE Quantum Leap Challenge Institute (Grant No. OMA-2016244); the V. Bush Fellowship; and the National Science Foundation (Grant No. PHY-2317149). This Letter is a contribution of the U.S. government, not subject to U.S. copyright.

Data availability—The data that support the findings of this Letter are available from the authors upon reasonable request.

[1] A. D. Ludlow, M. M. Boyd, J. Ye, E. Peik, and P. Schmidt, Rev. Mod. Phys. **87**, 637 (2015).
[2] BACON Collaboration, Nature (London) **591**, 564 (2021).
[3] H. N. Hausser *et al.*, Phys. Rev. Lett. **134**, 023201 (2025).
[4] M. S. Safronova, D. Budker, D. DeMille, D. F. J. Kimball, A. Derevianko, and C. W. Clark, Rev. Mod. Phys. **90**, 025008 (2018).
[5] M. S. Safronova, Ann. Phys. (Berlin) **531**, 1800364 (2019).
[6] N. Sherrill, A. O. Parsons, C. F. A. Baynham, W. Bowden, E. Anne Curtis, R. Hendricks, I. R. Hill, R. Hobson, H. S. Margolis, B. I. Robertson, M. Schioppo, K. Szymaniec, A. Tofful, J. Tunesi, R. M. Godun, and X. Calmet, New J. Phys. **25**, 093012 (2023).
[7] R. Lange, N. Huntemann, J. M. Rahm, C. Sanner, H. Shao, B. Lipphardt, C. Tamm, S. Weyers, and E. Peik, Phys. Rev. Lett. **126**, 011102 (2021).
[8] C. J. Kennedy, E. Oelker, J. M. Robinson, T. Bothwell, D. Kedar, W. R. Milner, G. E. Marti, A. Derevianko, and J. Ye, Phys. Rev. Lett. **125**, 201302 (2020).
[9] M. Filzinger, S. Dörscher, R. Lange, J. Klose, M. Steinel, E. Benkler, E. Peik, C. Lisdat, and N. Huntemann, Phys. Rev. Lett. **130**, 253001 (2023).
[10] C. W. Chou, D. B. Hume, T. Rosenband, and D. J. Wineland, Science **329**, 1630 (2010).
[11] T. Bothwell, C. J. Kennedy, A. Aeppli, D. Kedar, J. M. Robinson, E. Oelker, A. Staron, and J. Ye, Nature (London) **602**, 420 (2022).
[12] S. M. Brewer, J.-S. Chen, A. M. Hankin, E. R. Clements, C.-W. Chou, D. J. Wineland, D. B. Hume, and D. R. Leibrandt, Phys. Rev. Lett. **123**, 033201 (2019).
[13] Z. Zhiqiang, K. J. Arnold, R. Kaewuam, and M. D. Barrett, Sci. Adv. **9**, eadg1971 (2023).
[14] A. Aeppli, K. Kim, W. Warfield, M. S. Safronova, and J. Ye, Phys. Rev. Lett. **133**, 023401 (2024).
[15] N. Dimarcq *et al.*, Metrologia **61**, 012001 (2024).
[16] M. S. Safronova, M. G. Kozlov, and C. W. Clark, IEEE Trans. Ultrason. Ferroelectr. Freq. Control **59**, 439 (2012).
[17] Z. Y. Ma, K. Deng, Z. Y. Wang, W. Z. Wei, P. Hao, H. X. Zhang, L. R. Pang, B. Wang, F. F. Wu, H. L. Liu, W. H. Yuan, J. L. Chang, J. X. Zhang, Q. Y. Wu, J. Zhang, and Z. H. Lu, Phys. Rev. Appl. **21**, 044017 (2024).

[18] K. Cui, S. Chao, C. Sun, S. Wang, P. Zhang, Y. Wei, J. Yuan, J. Cao, H. Shu, and X. Huang, Eur. Phys. J. D **76**, 140 (2022).
[19] S. Hannig, L. Pelzer, N. Scharnhorst, J. Kramer, M. Stepanova, Z. T. Xu, N. Spethmann, I. D. Leroux, T. E. Mehlstäubler, and P. O. Schmidt, Rev. Sci. Instrum. **90**, 053204 (2019).
[20] C.-W. Chou, D. B. Hume, J. C. J. Koelemeij, D. J. Wineland, and T. Rosenband, Phys. Rev. Lett. **104**, 070802 (2010).
[21] P. O. Schmidt, T. Rosenband, C. Langer, W. M. Itano, J. C. Bergquist, and D. J. Wineland, Science **309**, 749 (2005).
[22] D. B. Hume, T. Rosenband, and D. J. Wineland, Phys. Rev. Lett. **99**, 120502 (2007).
[23] T. Rosenband, P. O. Schmidt, D. B. Hume, W. M. Itano, T. M. Fortier, J. E. Stalnaker, K. Kim, S. A. Diddams, J. C. J. Koelemeij, J. C. Bergquist, and D. J. Wineland, Phys. Rev. Lett. **98**, 220801 (2007).
[24] D. G. Matei, T. Legero, C. Grebing, S. Häfner, C. Lisdat, R. Weyrich, W. Zhang, L. Sonderhouse, J. M. Robinson, F. Riehle, J. Ye, and U. Sterr, J. Phys. Conf. Ser. **723**, 012031 (2016).
[25] T. Fortier and E. Baumann, Commun. Phys. **2**, 153 (2019).
[26] N. V. Nardelli, H. Leopardi, T. R. Schibli, and T. M. Fortier, Laser Photonics Rev. **17**, 2200650 (2023).
[27] J.-S. Chen, S. M. Brewer, C. W. Chou, D. J. Wineland, D. R. Leibrandt, and D. B. Hume, Phys. Rev. Lett. **118**, 053002 (2017).
[28] S. Stenholm, Rev. Mod. Phys. **58**, 699 (1986).
[29] D. J. Wineland, W. M. Itano, J. C. Bergquist, and R. G. Hulet, Phys. Rev. A **36**, 2220 (1987).
[30] A. M. Hankin, E. R. Clements, Y. Huang, S. M. Brewer, J.-S. Chen, C.-W. Chou, D. B. Hume, and D. R. Leibrandt, Phys. Rev. A **100**, 033419 (2019).
[31] See Supplemental Material at http://link.aps.org/supplemental/10.1103/hb3c-dk28 for additional details on evaluation of certain systematic shifts. Supplemental Material includes Refs. [32–35].
[32] Q. A. Turchette, D. Kielpinski, B. E. King, D. Leibfried, D. M. Meekhof, C. J. Myatt, M. A. Rowe, C. A. Sackett, C. S. Wood, W. M. Itano, C. Monroe, and D. J. Wineland, Phys. Rev. A **61**, 063418 (2000).
[33] W. M. Itano and D. J. Wineland, Phys. Rev. A **25**, 35 (1982).
[34] J. B. Wübbena, S. Amairi, O. Mandel, and P. O. Schmidt, Phys. Rev. A **85**, 043412 (2012).
[35] J. Keller, H. L. Partner, T. Burgermeister, and T. E. Mehlstäubler, J. Appl. Phys. **118**, 104501 (2015).
[36] M. E. Kim *et al.*, Nat. Phys. **19**, 25 (2023).
[37] K. Cui, J. Valencia, K. T. Boyce, E. R. Clements, D. R. Leibrandt, and D. B. Hume, Phys. Rev. Lett. **129**, 193603 (2022).
[38] J. Keller, H. N. Hausser, I. M. Richter, T. Nordmann, N. M. Bhatt, J. Kiethe, H. Liu, E. Benkler, B. Lipphardt, S. Dörscher, K. Stahl, J. Klose, C. Lisdat, M. Filzinger, N. Huntemann, E. Peik, and T. E. Mehlstäubler, J. Phys. Conf. Ser. **2889**, 012050 (2024).
[39] L. Pelzer, K. Dietze, V. J. Martínez-Lahuerta, L. Krinner, J. Kramer, F. Dawel, N. C. H. Spethmann, K. Hammerer, and P. O. Schmidt, Phys. Rev. Lett. **133**, 033203 (2024).
[40] D. Leibfried, R. Blatt, C. Monroe, and D. Wineland, Rev. Mod. Phys. **75**, 281 (2003).
[41] D. J. Wineland, C. Monroe, W. M. Itano, D. Leibfried, B. E. King, and D. M. Meekhof, J. Res. Natl. Inst. Stand. Technol. **103**, 259 (1998).
[42] S. M. Brewer, J.-S. Chen, K. Beloy, A. M. Hankin, E. R. Clements, C. W. Chou, W. F. McGrew, X. Zhang, R. J. Fasano, D. Nicolodi, H. Leopardi, T. M. Fortier, S. A. Diddams, A. D. Ludlow, D. J. Wineland, D. R. Leibrandt, and D. B. Hume, Phys. Rev. A **100**, 013409 (2019).
[43] H. C. J. Gan, G. Maslennikov, K.-W. Tseng, T. R. Tan, R. Kaewuam, K. J. Arnold, D. Matsukevich, and M. D. Barrett, Phys. Rev. A **98**, 032514 (2018).
[44] B. Efron, Ann. Stat. **7**, 1 (1979).
[45] T. Rosenband, W. M. Itano, P. O. Schmidt, D. B. Hume, J. C. J. Koelemeij, J. C. Bergquist, and D. J. Wineland, in *Proceedings of the 20th European Frequency and Time Forum* (IEEE, New York, 2006), pp. 289–292.
[46] Y.-F. Wei, S.-J. Chao, K.-F. Cui, C.-B. Li, S.-C. Yu, H. Zhang, H.-L. Shu, J. Cao, and X.-R. Huang, Phys. Rev. Lett. **133**, 033001 (2024).
[47] K. Beloy, D. R. Leibrandt, and W. M. Itano, Phys. Rev. A **95**, 043405 (2017).